A 2D Daubechies wavelet model on the vibration of rectangular plates containing strip indentations with a parabolic thickness profile

Li Ma, Su Zhang, Li Cheng[*]

Department of Mechanical Engineering, The Hong Kong Polytechnic University, Hong Kong

ARTICLE INFO

ABSTRACT

This paper presents a 2-D semi-analytical model for the vibration analyses of a plate with a power-law-profiled thickness variation, referred to as an Acoustic Black Hole (ABH) plate. The proposed model, along with the associated wavelet-based solution procedure, is intended to overcome major technical difficulties which are specific to ABH structures: the non-uniform wavelength distribution and ABH-induced wave compressions at the high frequency range in a realistic structure of finite size. Under the general Rayleigh-Ritz framework, Daubechies wavelet (DW) scaling functions are chosen as the admissible functions to decompose the transverse displacement of the plate with ABH indentations featuring a thickness variation along one direction of the panel. Modal and forced vibration analyses are carried out with results compared with those obtained by the FEM. It is shown that the model allows an accurate prediction of various vibration parameters and a realistic description of the typical ABH phenomena. Meanwhile, the use of Daubechies wavelet functions allows enhancing the effectiveness of the Rayleigh-Ritz method to reach the high frequency range, where systematic Acoustic Black Hole (ABH) effects are expected. Numerical analyses also reveal the potential of using strip ABH indentations in a plate to achieve a light-weight design with appealing vibration reduction properties. Analyses on the ABH-induced damping enhancement demonstrate the dominant effect of the local structural modes within indented area, which exhibit lower-order deformations (containing typically half and one wave along the direction in which the thickness is tailored).

1. Introduction

Research on acoustic black holes (ABHs) [1] has been attracting a growing attention in the last decade [2–8]. The phenomena, applicable to the propagating bending waves inside a thin-walled structure, features unique dynamic properties which promise great potential in applications such as vibration damping enhancement [9], energy harvesting [10] and sound radiation control [3,4] etc. through the use of light-weight structures.

Take a 1D case as an example, an ABH beam features a taper with a power-law profiled thickness variation, *i.e.*, $h(x) = \varepsilon x^\gamma$, where ε is a positive constant and γ a power law index, equal or larger than two [1]. Given an incident flexural wave travelling along the tapered beam, its phase velocity gradually reduces along the taper. In the ideal scenario, wave would stop travelling

---

* Corresponding author.
 E-mail address: li.cheng@polyu.edu.hk (L. Cheng).

at the zero-thickness tip of the taper without reflections, thus creating a strong energy concentration through wave compressions. In practical cases where a zero-thickness tip is not achievable, various measures to reduce wave reflections and to enhance energy dissipations have been extensively discussed in the literature [9,11].

The design of effective ABH structures relies on a good understanding of the underlying physics and a meticulous setting of the design parameters, be it material or geometrical. This can only be achieved with the help of efficient simulation and optimization tools. Up to now, extensive work has been carried out, predominantly using numerical tools such as finite element methods and experiments [2–4,12]. To a much less degree, effort has also been made to develop more physical models, aimed at capturing the fundamental features of the ABH phenomena using basic configurations. Typical examples include geometrical acoustics approach [13], graded impedance method [14], transfer matrix techniques [15], and impedance matrix techniques [16] etc. Pros and cons of these methods have been extensively discussed in previous works [17,18], among which geometrical and boundary restrictions of the structure as well as the applicable frequency range are the main concerns. More recently, structural modelling which considers more realistic structural features such as finite size, realistic structural boundaries and added-on damping layers has also been attempted, but mainly limited to 1D cases [18].

The modelling of the ABH structures is technically challenging due to the ABH-specific features, which are mainly twofold: a) structural wavelength varies significantly over a structure with embedded ABH elements. At any given frequency, bending waves experience a continuous wavelength variation and are severely compressed inside the ABH cells, while remaining relatively even over the uniform part of the structure; b) ABH effects start to systematically show only above the so-called cut-on frequency [4] or characteristic frequency [19], when the structural wave length starts to be comparable with the characteristic dimension of the ABH cells. Therefore, simulation methods should be able to reach the relatively high frequency range while being able to accommodate the significant wavelength variations over the structure. Along with these challenges, there is also the need in accommodating various structural changes such as add-on damping layers [18] or energy harvesting elements [10], as well as a better versatility and flexibility in coping with the structural design and optimizations. All these add further difficulties to the modelling task.

The use of wavelets under the Rayleigh-Ritz framework may provide a solution to cope with the aforementioned problems. In our previous work, a wavelet decomposed Rayleigh-Ritz method was proposed to model thin-walled structures with a constant thickness [20]. Results showed that the wavelet-based model can reach a much higher frequency range than the conventional Rayleigh-Ritz methods using admissible functions such as simple polynomials, Chebyshev series or trigonometric functions, which are prone to problems like numerical instability, ill condition or slow convergence [21,22]. Meanwhile, the unique features of the wavelets such as flexible scaling, compact support and strong fitting capability are shown to be conducive to the handling of ABH-specific wavelength variations. The idea was tested on a 1D beam using Mexican Hat Wavelets (MHWs) [18]. The formulation was rather straightforward since 1D configuration is relatively simple and MHWs can be analytically expressed. It was shown that the MHW-based Rayleigh-Ritz model allowed a good description of the ABH phenomena by accurately predicting the system dynamics at relatively high frequencies. Up to now, however, semi-analytical modelling of 2D ABH structures is scarce with the exception of a very recent work by O'Boy and Krylov [5]. That work follows the same Rayleigh-Ritz framework using trigonometric series as the admissible functions. The reported frequency range, however, is relatively low, typically covering the first twenty structural modes.

Inspired by our previous work on 1-D ABH beams [23] and the success in high frequency simulation on uniform structures [20], this paper proposes a 2D semi-analytical ABH model using Daubechies wavelet scaling functions. Compared with the MHWs which are smooth and analytically expressible, DWs are expected to better respond to the local variations of the ABH phenomena. However, as DW scaling functions have no closed form expressions, a proper recursive procedure needs to be worked out to deal with various operations on the scaling functions. In the present work, the same configuration used in O'Boy and Krylov [5] is adopted with an intention of improving that model to reach the effective ABH zone at much higher frequencies. The present paper is organized as follows. The proposed semi-analytical model is first developed for a plate with a strip ABH indentation in Section 2. In the formulation, DW scaling functions are chosen as the admissible functions for flexural displacement decomposition under the general Rayleigh-Ritz framework. Solutions to the derivatives of DW scaling functions and the connection coefficients are derived. In Section 3, numerical analyses on the first one hundred eigenfrequencies of the plate with free edges are carried out and validated using different support lengths and resolutions. Modal analyses and forced vibration analyses are then conducted for comparisons with the FEM simulations. In Section 4, typical ABH phenomena are illustrated using the developed model. Vibration reduction effects of the ABH plates are investigated with comparisons against a reference uniform plate. Changes in the modal loss factors are investigated and linked up with typical ABH cell modes. The energy focalization capacities of a strip ABH and a circular ABH are investigated and compared. Finally, conclusions are drawn.

2. Semi-analytical model and formulation

2.1. Modeling

As shown in Fig. 1(a), the investigated structure is a thin plate (with a dimension of *a, b,* and *h*), which contains a strip ABH indentation, symmetrically coated with damping layers on both sides. Fig. 1(b) gives the top view of the plate and Fig. 1(c) the cross-sectional thickness profile. The plate consists of two portions. The region containing the ABH strip is referred to as ABH portion, and the one with a constant thickness the uniform portion. The ABH portion is bounded by the range (x_1, x_2) and $(y_1,$
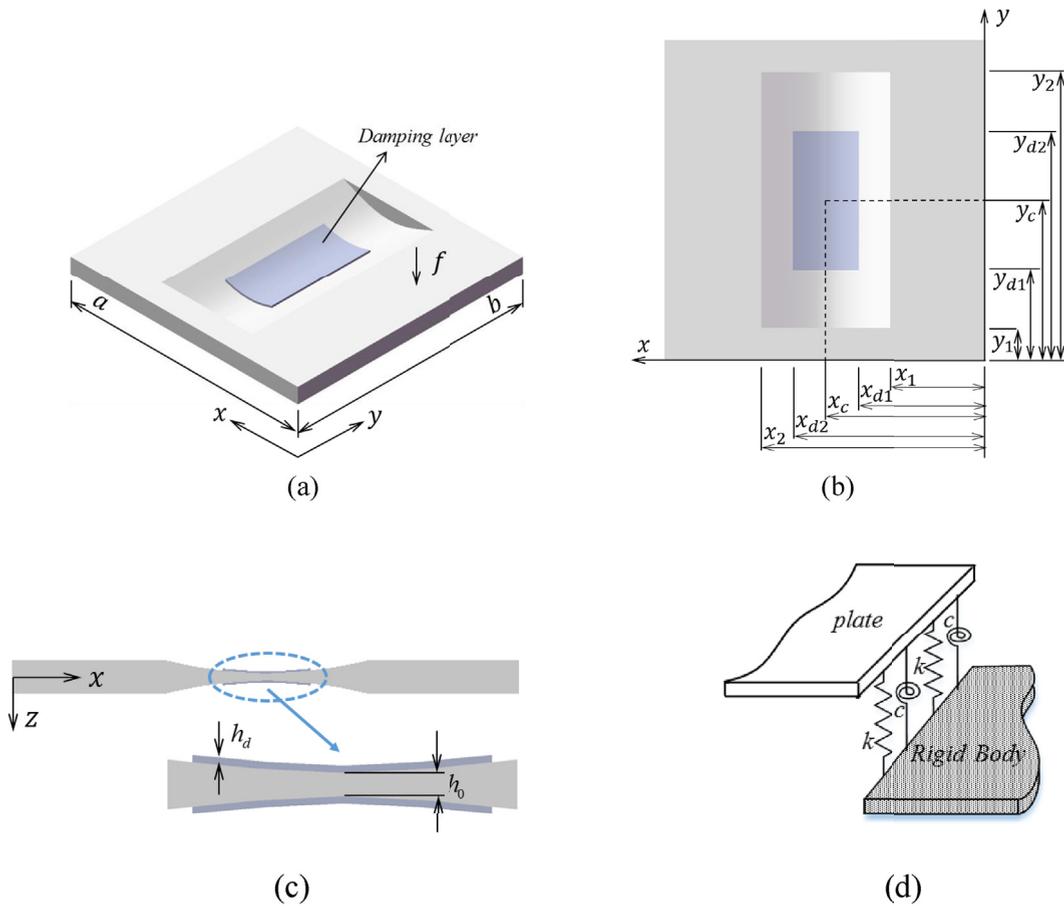
Fig. 1. Plate model: (a) Plate with symmetrical power-law thickness profiles; (b) ABH portion in vertical view; (c) Cross-section of the ABH portion; (d) Modeling of the boundary conditions.

y_2), centered at (x_c, y_c), featuring a thickness variation in x direction according to a power law realtion, *i.e.* $h(x) = \varepsilon(|x - x_c| + \delta)^\gamma$ with ε being a constant, γ a power law index and δ a parameter which determines the termination thickness in the thinnest middle part of the strip. Along the center at $x = x_c$, the ABH indentation has the smallest thickness $h_0 = \varepsilon\delta^\gamma$. Damping layers with a thickness h_d are coated within an area from x_{d1} to x_{d2} in x direction and from y_{d1} to y_{d2} in y direction. The boundary conditions of the plate are shown in Fig. 1(d). A set of springs working in translation and rotation are uniformly distributed along the edges of the plate [24] (k_i for translational spring stiffness and c_i for rotational spring stiffness with $i = 1, 2, 3, 4$ representing the edge number of the plate). The use of the springs allows various boundary conditions to be simulated through adjusting their stiffness values. Meanwhile, it allows a flexible choice of the admissible functions which are required to only satisfy the geometrical boundary conditions. The inherent material damping of the plate and that of the damping layers are introduced through complex Young's modulus $E_0 = E_0(1 + i\eta_0)$ and $E_d = E_d(1 + i\eta_d)$, respectively, where η_0 and η_d are the corresponding loss factors.

The system is assumed to be symmetrical with respect to the midplane of the plate. According to the Love-Kirchhoff thin plate theory, the displacement field of the system can be written as:

$$\{u, v, w\} = \left\{ -z\frac{\partial w}{\partial x}, -z\frac{\partial w}{\partial y}, w \right\} \tag{1}$$

in which vector $\{u, v, w\}$ contains the three displacements of a point, in either the plate or the damping layer.

Employing dimensionless coordinates $\xi = x/a$ and $\eta = y/b$, the transverse displacement w can be approximated by:

$$w = \sum_i^{\bar{p}} \sum_j^{\bar{q}} a_{ij}(t)\varphi_i(\xi)\varphi_j(\eta) \tag{2}$$

where $\varphi_i(\xi)$ and $\varphi_j(\eta)$ are the assumed admissible functions and $a_{ij}(t)$ are the unknown complex coefficients; $\bar{p}$ and $\bar{q}$ are the truncation order representing the number of terms of admissible functions to be kept in the computation; $a_{ij}(t)$ are the generalized coordinates in the Euler-Lagrange equations which result from the stationary state of the system:

$$\frac{d}{dt}\left(\frac{\partial \mathscr{L}}{\partial \dot{a}_{ij}(t)}\right) - \frac{\partial \mathscr{L}}{\partial a_{ij}(t)} = 0. \tag{3}$$

where $\mathscr{L}$ is the Lagrangian operator written as:

$$\mathscr{L} = E_k - E_p + W \tag{4}$$

in which E_k and E_p are the kinetic energy and the potential energy of the system, respectively; and W the work done by external forces. Neglecting small quantities of higher orders, these terms are expressed as:

$$E_k = \frac{1}{2}\rho ab \int \int h(\xi)\left(\frac{\partial w}{\partial t}\right)^2 d\xi d\eta$$

$$E_p = \frac{1}{2}\int \int \frac{E[h(\xi)]^3}{12(1-\mu^2)}\left[\begin{array}{c} \dfrac{b}{a^3}\left(\dfrac{\partial^2 w}{\partial \xi^2}\right)^2 + \dfrac{a}{b^3}\left(\dfrac{\partial^2 w}{\partial \eta^2}\right)^2 \\[4mm] +2\mu\dfrac{1}{ab}\left(\dfrac{\partial^2 w}{\partial \xi^2}\dfrac{\partial^2 w}{\partial \eta^2}\right) + 2(1-\mu)\dfrac{1}{ab}\left(\dfrac{\partial^2 w}{\partial \xi \partial \eta}\right)^2 \end{array}\right] d\xi d\eta$$

$$+\frac{b}{2}\int_0^1\left\{\begin{array}{c} k_1[w(0,\eta,t)]^2 + k_2[w(1,\eta,t)]^2 \\[4mm] +c_1\cdot\dfrac{1}{a^2}\left[\dfrac{\partial w(\xi,\eta,t)}{\partial \xi}\bigg|_{\xi=0}\right]^2 + c_2\cdot\dfrac{1}{a^2}\left[\dfrac{\partial w(\xi,\eta,t)}{\partial \xi}\bigg|_{\xi=1}\right]^2 \end{array}\right\}d\eta \tag{5}$$

$$+\frac{a}{2}\int_0^1\left\{\begin{array}{c} k_3[w(\xi,0,t)]^2 + k_4[w(\xi,1,t)]^2 \\[4mm] +c_3\cdot\dfrac{1}{b^2}\left[\dfrac{\partial w(\xi,\eta,t)}{\partial \eta}\bigg|_{\eta=0}\right]^2 + c_4\cdot\dfrac{1}{b^2}\left[\dfrac{\partial w(\xi,\eta,t)}{\partial \eta}\bigg|_{\eta=1}\right]^2 \end{array}\right\}d\xi$$

$$W = f(t)w\left(\xi_f,\eta_f,t\right)$$

where ρ is the density, μ the Poisson's ratio and (ξ_f,η_f) the location of the excitation force. Integrals in Eq. (5) should be evaluated for the whole system, including both the plate and the damping layers. Application of Eqs. (4) and (5) to Eq. (3) leads to a set of linear equations, expressed in a matrix form as:

$$\mathbf{M}\ddot{\mathbf{a}}(t) + \mathbf{K}\mathbf{a}(t) = \mathbf{F}(t) \tag{6}$$

where $\mathbf{M}$ and $\mathbf{K}$ represent the global mass and stiffness matrices (complex due to viscoelasticity of the material), respectively. The entire structure is divided into five parts. The formation of $\mathbf{K}$ and $\mathbf{M}$ is given in Appendix A.

Considering a harmonic excitation, Eq. (6) can be cast into the standard matrix form. Dropping the excitation terms yields a standard eigenvalue problem for free vibration analyses, whose solution gives the natural frequencies of the system along with the corresponding mode shapes. As $\mathbf{K}$ is complex, the natural angular frequencies are also in a complex form as:

$$\omega^2 = \omega_n^2(1 + i\eta_n) \tag{7}$$

where ω_n are the natural angular frequencies and η_n the corresponding modal loss factors. η_n is an important parameter to characterize the energy dissipation of individual resonant modes resulting from the ABH effects, which will be described later on.

2.2. Daubechies wavelet scaling functions

As shown in Appendix A, expressions of the stiffness matrix $\mathbf{K}$ and mass matrix $\mathbf{M}$ require the handling of some finite integral terms involving the DW scaling functions and their derivatives. This is worked out in this Section. For the benefit of the readership, Daubechies wavelets are briefly recalled and discussed. DWs are a compactly supported and orthogonal set which can be scaled to accommodate both localized and smooth variations [25]. Each DW member is governed by an even integer L and a set of wavelet filter coefficients $\{p_l,\ l = 0, 1, 2, \ldots L-1\}$ through a two-scale relation:

$$\varphi(x) = \sum_{l=0}^{L-1} p_l \varphi(2x - l) \tag{8}$$

and

$$\psi(x) = \sum_{l=2-L}^{1} (-1)^l p_{1-l} \varphi(2x - l) \tag{9}$$

where $\varphi(x)$ is the scaling function and $\psi(x)$ the mother wavelet. Note $\varphi(x)$ and $\psi(x)$ are completely localized in the interval [0, $L - 1$] and [$1 - L/2, L/2$], respectively. The conditions that the coefficients p_j need to satisfy can be found in Ref. [25].

The constructed $\psi(x)$ possesses the following property:

$$\int_{-\infty}^{+\infty} x^k \psi(x) dx = 0 \qquad k = 0, 1, ..., L/2 - 1 \tag{10}$$

which indicates that the elements of the set $\{1, x, ..., x^{L/2-1}\}$ can be a linear combination of $\varphi(x - k)$, translated from $\varphi(x)$ by k. Also, the nth derivative of the scaling function $\varphi^{(n)}(x)$ exists for $n = 0, 1, ..., L/2 - 1$. Employing Eq. (8), an analogous form of the two-scale relation for $\varphi^{(n)}(x)$ can be obtained as:

$$\varphi^{(n)}(x) = 2^n \sum_{l=0}^{L-1} p_l \varphi^{(n)}(2x - l) \tag{11}$$

Eq. (11) allows the calculations of the values of $\varphi^{(n)}(x)$ for all dyadic points at $x = k/2^j$, when $\varphi^{(n)}(k)$ are known at the integer points $k = 1, 2, ..., L - 2$. Substituting these integer points into Eq. (11) gives a system of linear equations as:

$$2^{-n}\mathbf{\Phi} = \mathbf{P}\mathbf{\Phi} \tag{12}$$

where

$$\mathbf{\Phi} = \left[\varphi^{(n)}(1), \varphi^{(n)}(2), ..., \varphi^{(n)}(L - 2) \right]^{\mathrm{T}} \tag{13}$$

in which superscript T denotes the transpose and $\mathbf{P}$ is a $(L - 2) \times (L - 2)$ matrix:

$$\mathbf{P} = \left[p_{2l_1 - l_2} \right]_{1 \le l_1, l_2 \le L-2} \tag{14}$$

with l_1 and l_2 being the row and column indices, respectively. Vector $\mathbf{\Phi}$, the eigenvector, can be uniquely determined with the following normalization condition [25]:

$$\sum_{k=1}^{L-2} (-k)^n \varphi^{(n)}(k) = n! \tag{15}$$

Upon getting values of $\varphi^{(n)}(k)$ at $k = 1, 2, ..., L - 2$, values of $\varphi^{(n)}(x)$ at $x = k/2^j$ for $k = 1, 3, 5, ..., 2^j(L - 1) - 1$ and $j = 1, 2, ...$ can be determined by using the relation:

$$\varphi^{(n)}\left(\frac{k}{2^j}\right) = 2^n \sum_{l=0}^{L-1} p_l \varphi^{(n)}\left(\frac{k}{2^{j-1}} - l\right) \tag{16}$$

knowing that $\varphi^{(n)}(x) = 0$ for $x \le 0$ and $x \ge L - 1$.

2.3. Connection coefficients

Write the 2D wavelet base functions in the ξ and η directions as $\varphi_i(\xi) = 2^{m/2}\varphi(2^m\xi - i)$ and $\varphi_j(\eta) = 2^{m/2}\varphi(2^m\eta - j)$, respectively, where m is the resolution, i and j are the corresponding translations. To avoid the singularity when solving Eq. (6), i and j should be confined to the range $[-L + 2, ..., 2^m - 1]$. This leads to a total of number of terms given by $\bar{p} = \bar{q} = 2^m + L - 2$. All the wavelet terms located within the interval [0, $L - 1$] should be included in the displacement field.

For the purpose of illustration, $\varphi_i(\xi)$ with $m = 2$ and $i = -3, ..., 3$ is shown in Fig. 2.

As shown in Appendix A, constructing $\mathbf{K}$ and $\mathbf{M}$ for each part of the plate (numbered by $q = 1, 2, ..., 5$ in Appendix A) requires the calculations of 2-D connection coefficients which are the finite integrals involving admissible functions and their
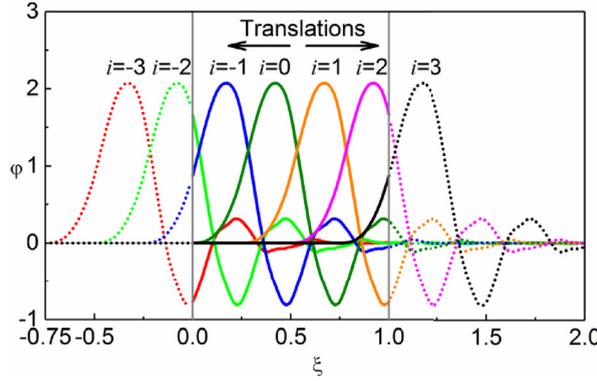
Fig. 2. Daubechies scaling functions with $L = 12$, $m = 2$, $i = -3, ..., 3$.

derivatives. The terminology of the so-called connection coefficients has been widely used in the literature on various applications of wavelets [20]. In the present case, the general form of 2D connection coefficients writes:

$$I_{r,i,s,j} = \int\limits_{\eta_{q1}}^{\eta_{q2}} \int\limits_{\xi_{q1}}^{\xi_{q2}} [h(\xi)]^n \varphi_r^{(\alpha_\xi)}(\xi) \varphi_i^{(\beta_\xi)}(\xi) \varphi_s^{(\alpha_\eta)} \varphi_j^{(\beta_\eta)}(\eta) d\xi d\eta \tag{17}$$

where ξ_{q1} and ξ_{q2} are, respectively, the lower and upper limits in ξ direction for a given part of the plate q; and η_{q1} and η_{q2} in η direction. n can be 1 or 3.

Due to the geometry of the strip ABH indentation, integrals in Eq. (17) are separable. Recalling $\xi = x/a$ and $\eta = y/b$, $\varphi^{(\alpha)}(x) = (1/a)^\alpha \cdot \varphi^{(\alpha)}(\xi)$ and $\varphi^{(\beta)}(y) = (1/b)^\beta \cdot \varphi^{(\beta)}(\eta)$. The general forms of 1D connection coefficients, $\mathbf{I}_x$ and $\mathbf{I}_y$ in the x and y directions, can be written as:

$$I_{x,r,i}^{\alpha,\beta} = (1/a)^{\alpha-1}(1/b)^\beta 2^{(\alpha+\beta)m} \int\limits_{\xi_{q1}}^{\xi_{q2}} [h(\xi)]^n \cdot 2^{m/2}[\varphi(2^m\xi - r)]^{(\alpha)} \cdot 2^{m/2}[\varphi(2^m\xi - i)]^{(\beta)} d\xi$$

$$I_{y,s,j}^{\alpha,\beta} = (1/a)^\alpha (1/b)^{\beta-1} 2^{(\alpha+\beta)m} \int\limits_{\eta_{q1}}^{\eta_{q2}} 2^{m/2}[\varphi(2^m\eta - s)]^{(\alpha)} \cdot 2^{m/2}[\varphi(2^m\eta - j)]^{(\beta)} d\eta \tag{18}$$

where $\varphi^{(\alpha)}$ and $\varphi^{(\beta)}$ (with $\alpha, \beta = 0, 1, 2$) are the derivatives of the scaling functions, which can be obtained by following the procedure described in Section 2.2. Finally, the 2D connection coefficients are decomposed as a tensor product of their 1D counterparts $\mathbf{I}_x$ and $\mathbf{I}_y$ as:

$$\mathbf{I} = \mathbf{I}_x \otimes \mathbf{I}_y \tag{19}$$

where $\otimes$ is the Kronecker tensor product symbol. Integrations in Eq. (18) can then be carried out using 1D Gauss integration method.

It is relevant to note that the established formulation and the associated numerical scheme also apply to plates with circular ABH indentations. In that case, the thickness of the plate is a function of both ξ and η. Therefore, Eq. (17) should be rewritten as:

$$I_{r,i,s,j} = \int\limits_{\eta_{q1}}^{\eta_{q2}} \int\limits_{\xi_{q1}}^{\xi_{q2}} [h(\xi,\eta)]^n \varphi_r^{(\alpha_\xi)}(\xi) \varphi_i^{(\beta_\xi)}(\xi) \varphi_s^{(\alpha_\eta)} \varphi_j^{(\beta_\eta)}(\eta) d\xi d\eta \tag{20}$$

As a result, terms involving ξ and η are inseparable and the integral should be calculated by the 2-D Gauss integration.

Table 1
Geometrical and material parameters.

Geometry		Material
$a = 0.56$ m	$y_1 = 0.056$ m	$E_0 = 200$ GPa
$b = 0.56$ m	$y_2 = 0.504$ m	$\mu_0 = 0.3$
$h = 6.4$ mm	$h_0 = 0.4$ mm	$\eta_0 = 0.01$
$x_1 = 0.16$ m	$\varepsilon = 0.25$	$\rho_0 = 7800$ kg/m^3
$x_2 = 0.4$ m	$\gamma = 2$	
$x_c = 0.28$ m	$\delta = 0.04$ m	
$y_c = 0.28$ m		

3. Numerical implementations and model validations

3.1. Determination of DW parameters and model validations

The accuracy of the proposed model is first verified through comparisons with the FEM simulations. Wavelet parameters are varied in order to determine a suitable combination to be used in the subsequent analyses for the maximum calculation efficiency and the required accuracy. To this end, the eigen-frequencies of a typical ABH plate are calculated using different L and m values. Geometrical and material parameters of the plate as well as those of the ABH indentation are tabulated in Table 1. The four edges of the plate are set to be free, by assigning a zero stiffness value to all the boundary springs. The FEM model using COMSOL software is densely meshed with an element size of 0.005 m to ensure the convergence of the solution. This gives a total of 12544 plate elements.

Note that Eq. (10) involves the derivative terms of the DWs up to an order of $L/2 - 1$. Therefore, L should be at least equal to or larger than 10 [20]. Firstly, with L fixed at 12, the influences of m are analyzed. Three typical m values, 6, 7 and 8, are used in the calculation which gives a total of 5476, 19044 and 70756 wavelet terms, respectively. The calculated eigen-frequencies of the first 100 modes are compared with those obtained by FEM in Fig. 3. It can be seen that results with $m = 7$ and 8 agree well with FEM results within the entire mode range, while more noticeable deviations in the higher-order modes appear when $m = 6$. To quantify the calculation accuracy, the relative error, defined as $|f_{model} - f_{FEM}|/f_{FEM} \times 100\%$, are calculated and shown
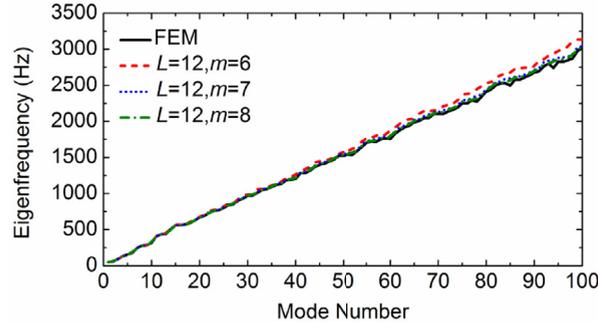
Fig. 3. Comparisons with FEM analyses for the first 100 eigen-frequencies: FEM (solid line); $L = 12$, $m = 6$ (short dash line); $L = 12$, $m = 7$ (short dot line); $L = 12$, $m = 8$ (short dash dot line).
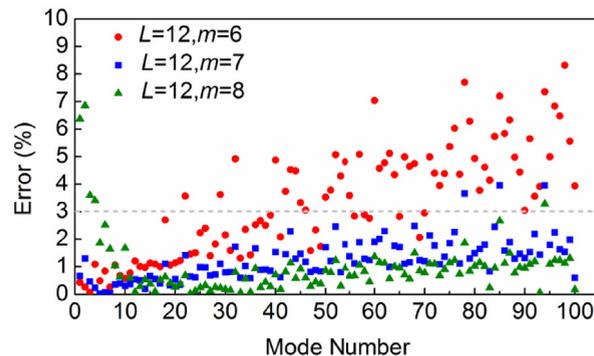
Fig. 4. Percent errors for the first 100 eigen-frequencies obtained by the present model with $L = 12$: $m = 6$ (circle dot); $m = 7$ (square dot) and $m = 8$ (triangle dot).
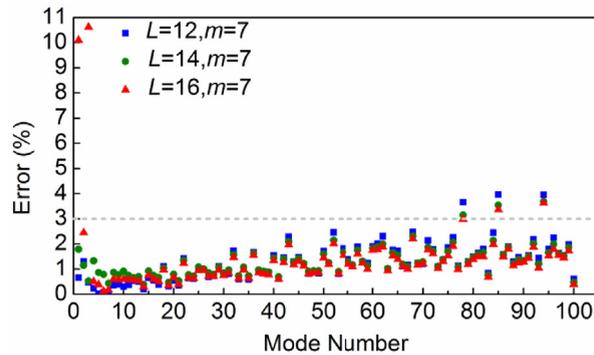
Fig. 5. Percent errors for the first 100 eigen-frequencies obtained by the present model with $m = 7$: $L = 12$ (square dot); $L = 14$ (circle dot) and $L = 16$ (triangle dot).

in Fig. 4. Results confirm the same trend as the one observed in Fig. 3. Typically, $m = 7$ or 8 with $L = 12$ allows limiting the error below 3% for a large majority of modes. Clearly, a larger m (*e.g.* $m = 8$) leads to a better accuracy for higher order modes, except for the first few modes. Similar phenomenon was also observed in a previous study using MH wavelets in 1D cases [18], which can be explained by the scaling properties of the wavelets. This suggests that a larger m is preferable for higher order mode prediction, which is the main frequency range of interest where systematic ABH effect is expected. Fixing m at 7 and varying L, the calculation errors against FEM results are given in Fig. 5. As can be seen, the three cases give very similar accuracy, except for the very low-order modes.

Apart from the accuracy, it is also relevant to consider the computation time which is mainly determined by the scaling factor m. For example, for a fixed L, the computation time for $m = 8$ is four times that of $m = 7$. Therefore, based on the above analyses, a calculation scheme using $L = 12$ and $m = 7$ is taken as a good compromise, from both the accuracy and the computation time perspectives. This will be used in the subsequent analyses.

Fig. 6 compares three arbitrarily chosen mode shapes, *i.e.*, the 50th, 79th and 98th modes, obtained by the present model and the FEM. It can be seen that, the proposed model allows a fine description of the vibrational details, including the local deformation within the ABH indentation area. Both sets of results seem to agree well, further confirming the remarkable ability of the proposed model in describing ABH-specific features even for higher-order modes.

A forced vibration analysis is further carried out. A unit harmonic excitation force is applied at point $(\xi_f, \eta_f) = (1/7, 1/2)$ on the uniform portion of the plate. The mean square velocities, spatially averaged over the ABH portion and the uniform portion of the plate, respectively, are calculated and compared with the FEM results in Fig. 7. It can be seen that, with the L and m combination suggested above, results calculated by the present model are in good agreement with those from the FEM analysis.

To sum up, above comparisons show that the proposed model provides results which are consistent with FEM results, in terms of both modal characteristics and forced vibration responses. Most importantly, the model allows reaching the effective high frequency range, relevant to the ABH investigations. In fact, the frequency range outreach of the method well exceeds the conventionally reachable range using Rayleigh-Ritz models reported in the literature, demonstrating the attractiveness of the Daubechies scaling functions as a global basis.

4. Numerical analyses and discussions

4.1. ABH phenomena and vibration benefit

Typical ABH phenomena, in terms of the compressed wavelength and increased vibration amplitude, are first analyzed using the same free plate. Note the issue of addressing other types of boundary conditions using Rayleigh-Ritz method has been extensively discussed in the literature [20]. It was observed (not shown here) that the boundary conditions do not fundamentally change the typical ABH phenomena that will be reported hereafter using a freely supported plate. In this case, the ABH strip covers the entire y direction of the plate. Fig. 8(a) shows a cross sectional view along the x-axis of a typical mode shape (92th order) obtained by the present model. It can be seen that the wavelength begins to decrease at the interface between the uniform portion and the ABH portion. Meanwhile, the vibration amplitude gradually increases, typical of the expected ABH feature. After ABH cell modes cut on, the ABH cell is expected to interact with the incident bending wave to create a significant vibration energy shift to the ABH portion. This is quantified by the ratio of the mean square velocity of the ABH portion to that of the uniform portion, defined as $\Gamma = 10 \log_{10} \left(\frac{<v_{ABH}^2>}{<v_{uniform}^2>} \right)$. A larger Γ signifies a greater energy concentration in the ABH portion. Fig. 8(b) shows a clear vibration energy shift from the uniform portion to the ABH portion as a result of typical ABH effect, leading to a strong energy focalization within the ABH strip. This ABH-induced feature is

(a)

(b)

(c)
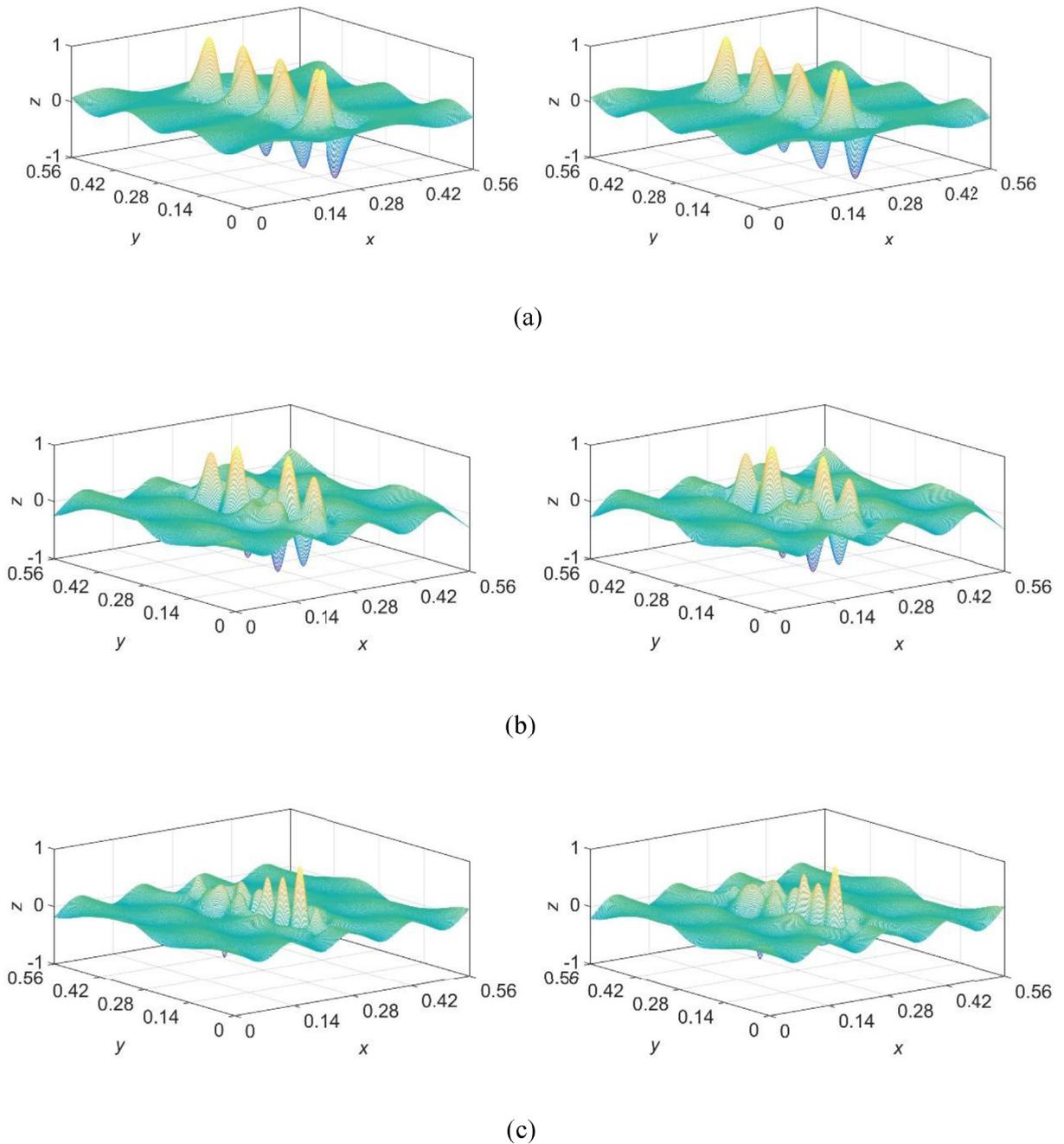
Fig. 6. Mode shape comparisons: Present model (left); FEM (right). (a) mode 50; (b) mode 79; (c) mode 98.

conducive to energy harvesting and vibration reduction through local damping enhancement. Results also demonstrate that the present model correctly captures the main ABH-specific features of the plate.

To investigate the potential of using a strip ABH for vibration reductions, damping layers are symmetrically placed with respect to the central line of the strip (see Fig. 9(b)), from $x_{d1} = 0.25$ m to $x_{d2} = 0.31$ m and from $y_{d1} = 0$ to $y_{d2} = 0.56$ m, with a constant thickness of $h_d = 2h_0$. The damping material has a Young's modulus $E_d = 5$ GPa, a density $\rho_d = 950$ kg/m^3 and a Poisson ratio $\mu_d = 0.3$. Plate parameters are the same as those used before, tabulated in Table 1. The total mass of the added damping layers is 0.26% that of the plate. For comparisons, a reference flat plate of the same size (coated with the same amount of damping layers at the same corresponding location, shown in Fig. 9(a)) is also considered.

Under the same mechanical excitation, the mean square velocities averaged over the uniform portion of the two plates are compared in Fig. 10. It can be seen that the vibration level of the plate with the ABH indentation is generally much lower than
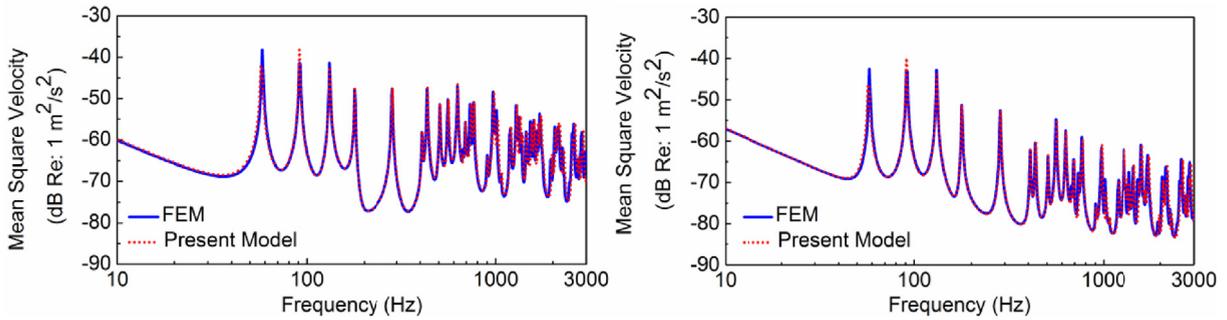
Fig. 7. Mean square velocity: ABH portion (left); Uniform portion (right).

(a)   (b)
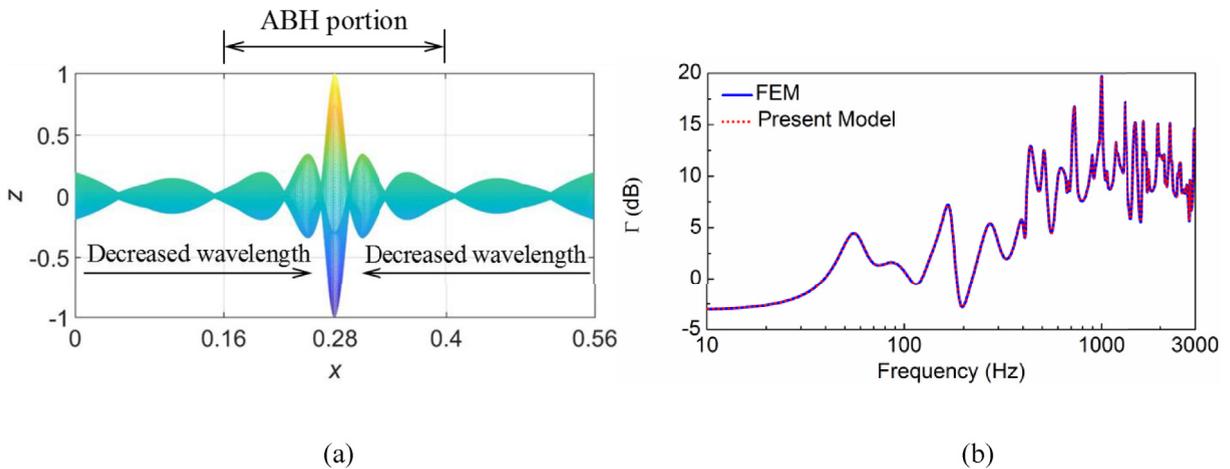
Fig. 8. Typical ABH features: (a) Decreased wavelength towards the center of ABH portion; (b) Ratio of the mean square velocity between the ABH portion and that of the uniform portion.

that of its flat counterpart. Typically, peak levels differ by up to 12 dB. This shows the benefit of tailoring an ABH strip by removing materials from a flat panel to make the structure lighter and more vibration appealing at the same time, as far as the uniform part of the plate is concerned.

The aforementioned phenomena can be better explained by investigating the effects of the damping layers on each plate. Fig. 11(a) shows that, due to the rather uniform energy distribution in the flat plate, the use of the small amount of damping layers turn out to be insignificant, barely visible for some particular resonances. As to the ABH-featured plate, however, the same amount of damping leads to a much more visible vibration reduction, as demonstrated in Fig. 11(b). The vibration reduction is more obvious and systematic at higher frequencies, typically above the characteristic frequency of 500 Hz, where incident flexural waves interact more effectively with the ABH indentation due to their shorter wavelengths compared to the size of the ABH cell. This is also consistent with previous studies on 1D ABH wedges [8,17] which showed that the impaired ABH effect caused by the thickness truncations can be well compensated by using a small piece of damping layer coated on the tapered ABH region. The presence of the damping layers largely reduces the reflection coefficient, thus leading to a more significant energy concentration and dissipation in the tapered ABH region.

4.2. Modal loss factors

The bi-dimensionality of an ABH plate is expected to exhibit different features as compared to a 1D ABH taper. This is scrutinized by examining the overall modal loss factors of the strip ABH plate. Upon the deployment of the damping layers over the strip ABH plate, same as above, Fig. 12 depicts the calculated modal loss factors for the first 100 structural modes. Note that, as compared with the inherent material damping (0.01 for the plate), one notices a significant damping increase for most modes, consistent with the observations made in 1D structures [18]. However, different from the 1D case where damping enhancement is systematic for all modes with roughly the same enhancement level above the characteristic frequency, the current 2D plate exhibits a much more scattered pattern in terms of damping enhancement. More specifically, the cloud points in Fig. 12 seem to regroup into different clusters, each following a different variation trend with respect to the increasing mode number/frequency. Typical mode shapes in each group are shown in Fig. 12. The first group of modes seem to

Fig. 9. Reference plate and ABH plate coated with the same amount of damping layers. Coating area $x_{d1} \sim x_{d2} = 0.25 - 0.31$ m, $y_{d1} \sim y_{d2} = 0 - 0.56$ m and thickness $h_d = 2h_0$: (a) Reference plate; (b) ABH plate. Dark gray area denotes the area coated with damping layers.
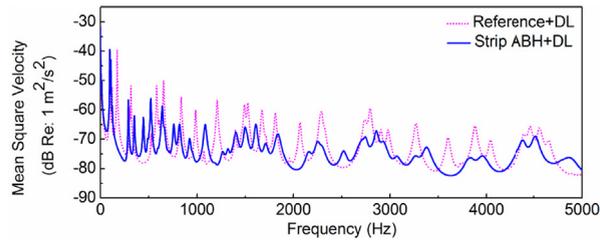
Fig. 10. Mean square velocity of uniform portion: Reference plate with damping layers (dot line); Strip ABH plate with damping layers (solid line).
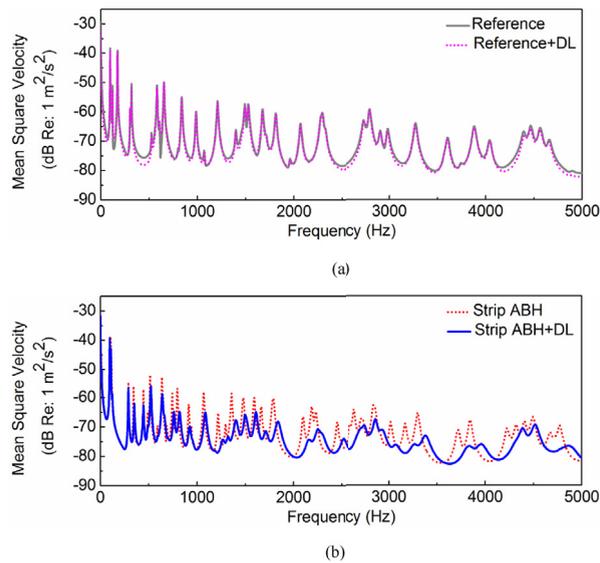
Fig. 11. (a). Mean square velocity of the uniform portion of reference flat plate: Without damping layers (solid line); With damping layers (dot line). (b). Mean square velocity of the uniform portion of Strip ABH plate: Without damping layers (dot line); With damping layers (solid line).

follow an obvious monotonically increasing trend with the frequency, with significantly topped-up damping. Mode shapes show that these modes share the common feature of having a half-wave along the x-direction (thickness tailoring direction) of the ABH strip, denoted as (1, n) modes. The following group with a moderate damping increase consists of (2, n) modes, with a full wave contained within the ABH strip in the x-direction. With the further increase in the structural deformation within the ABH cells along x-direction, the increase of the modal loss factors of the plate further diminishes. At the bottom of the cloud points are these modes involving a global structural deformation of the plate. When this happens, the deployed damping layers within the small ABH region cannot generate meaningful damping increase in the overall structure. Therefore, the observed overall damping increase, brought up by the viscoelastic coating, as well as the vibration reduction phenomena observed in Fig. 11(b), is mainly attributed to the significant damping enhancement of the lower order local ABH modes, typically these involving a half and one wave in the direction in which the plate thickness profile is tailored.

4.3. Strip ABH versus circular ABH

It is surmised that bi-dimensionality properties of ABH plates would be better seen with a circular ABH indentation, since its local thickness variation might generate more pronounced coupling effects between the x and y directions of the plates. As aforementioned, apart from some mathematically treatments which are specific to the calculation of the energy terms, the
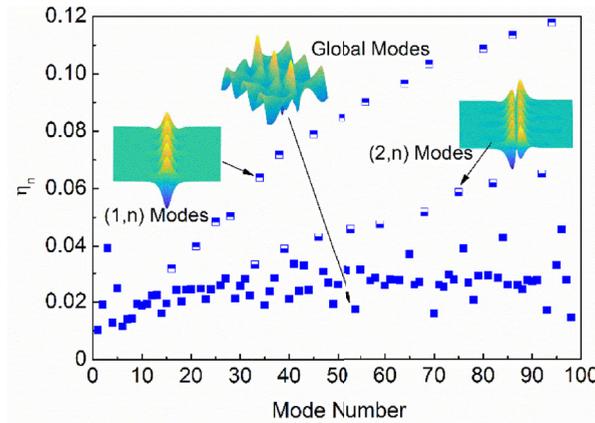
Fig. 12. Modal loss factors of the strip ABH plate coated with damping layers: (1, n) ABH cell modes (dots with hollow lower part); (2, n) ABH cell modes (dots with hollow upper part); Global modes (solid dots).
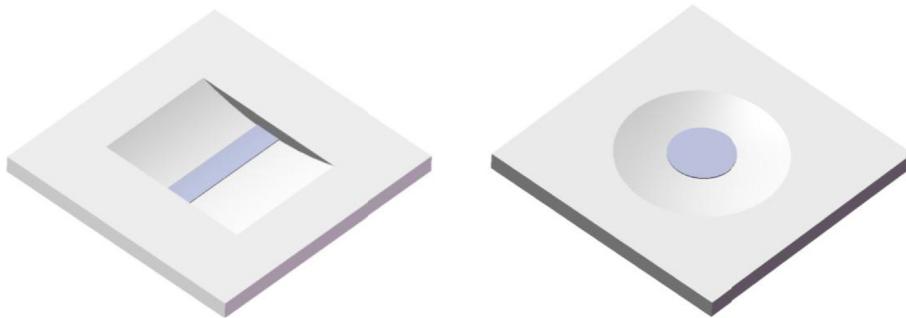
Fig. 13. Plates with two types of ABH indentations: Strip (left); Circular (right). Dark gray area denotes the area coated with damping layers.

proposed modelling approach is also valid for plates embedded with a circular indentation, shown in Fig. 13. Using the model, a strip ABH plate and a circular ABH plate are compared in terms of energy concentration. While the local thickness variation of the strip ABH being $h(x) = \varepsilon(|x - x_c|)^\gamma + h_0$, that of the circular indentation follows $h(r) = \varepsilon r^\gamma + h_0$, where r is the radial coordinate of the circular ABH indentation. For comparisons, the dimensions of these two plates are chosen to be the same: $a = 0.5$m, $b = 0.5$m, $h = 4.7$mm. Parameters for both ABH indentation are $\varepsilon = 0.2$, $\gamma = 2$ and $h_0 = 0.2$mm. The circular indentation has a radius $R_{ABH} = 0.15$ m. To ensure the same area for both indentations, the dimension of the strip ABH is determined, covering an area from $x_1 = 0.1$ m to $x_2 = 0.4$ m in x direction and from $y_1 = 0.13225$m to $y_2 = 0.36775$m in y direction. Similarly, the same amount of damping material, 0.146% of the bare reference plate, is used around the center of both ABH indentations. For comparison purposes, the mean square velocity ratio Γ and the overall loss factors of each plate are calculated and compared.
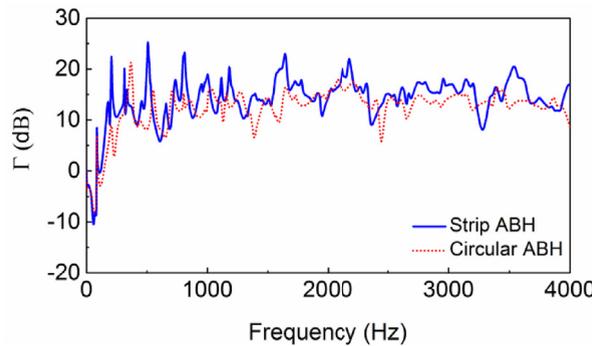
Fig. 14. Comparison of the ratio of the mean square velocity between the ABH portion and that of the uniform portion without damping layers: Strip ABH plate (solid line); Circular ABH plate (dot line).
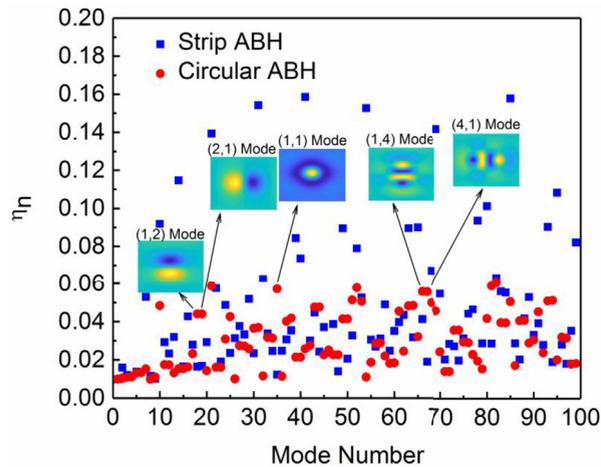
Fig. 15. Comparison of the modal loss factors of the strip ABH plate and the circular ABH plate with damping layers: Strip ABH plate (square dot); Circular ABH plate (circular dot).

In the absence of the damping layers, Fig. 14 shows that, above the characteristic frequency (500 Hz), the strip ABH plate seems to be generally superior to its circular counterpart in terms of energy focalization. The overall ABH effect is also confirmed by Fig. 15 in that, upon using the damping layers, the overall loss factors of most the strip ABH modes are also much larger than those of circular ABH.

The dynamics of the circular ABH plate can be better understood by examining the local deformation of the ABH indentations. Having understood the relationship between the damping loss factor with the local mode shapes in the case of the strip ABH plate, the same analysis is now carried out for the circular one. Similar to the strip ABH plate, Fig. 15 shows that the largest damping increase also corresponds to the local ABH modes in the circular ABH plate. Different from the strip ABH plate, for which $(1, n)$ modes have larger modal loss factors than $(2, n)$ modes, for the circular ABH plate, local ABH $(1, 2)$ and $(2, 1)$ modes seem to provide very similar modal loss factors. Same applied to modes $(1, 4)$ and $(4, 1)$. This is naturally due to the bi-dimensionality of the circular ABH indentation. In the case of the circular ABH indentation, as opposed to the strip case, mode classifications seem to be more difficult, although results still suggest that significant damping enhancement is governed by the lower order local ABH modes.

5. Conclusions

In this paper, a semi-analytical 2D model is proposed for the vibration analyses of rectangular plates containing strip ABH indentations with a parabolic thickness profile. Under the general Rayleigh-Ritz framework, Daubechies wavelet scaling functions are employed to decompose the transverse displacement of the plate with ABH indentations featuring a thickness variation along one direction of the panel. The proposed mathematical treatment establishes the general formalism of the modelling, including the derivation and the calculation of the connection coefficients of the Daubechies wavelet scaling functions which are not analytically expressible. Numerical analyses lead to the following conclusions:

1). The proposed model, as well as the associated wavelet-based solution procedure, is shown to be able to overcome major technical difficulties which are specific to ABH structures: non-uniform wavelength distribution and ABH-induced wave compressions in the high frequency range in a realistic structure of finite size. More specifically, comparisons with FEM simulations show that the proposed model can produce accurate results in terms of the natural frequencies (with errors typically capped below 2–3%), mode shapes as well as the forced vibration responses, up to a frequency range governed by roughly the first 100 modes. The accuracy, as well as the frequency outreach well exceeds similar work reported in the literature. In that sense, this work offers a useful model which is conducive to the study of ABH phenomena.

2). Numerical analyses show typical energy focalization and dissipation phenomena of a plate with embedded ABH indentation covered by a small amount of damping materials, pointing at the possibility of designing light-weight structures with better vibration reduction performance. It is shown that, above the characteristic frequency of the panel, the ABH-induced damping enhancement phenomenon is mainly attributed to the local structural modes within the ABH indentation. These modes exhibit lower-order deformations (typically half and one wave along the thickness tailoring direction) for the strip indentation. Contributions to the damping increase by the higher-order local modes along the thickness tailoring direction and global modes are trivial and negligible. Owing to the high structural modal density, this turns out to be enough to produce an appreciable damping increase, and subsequent a vibration reduction

of the entire structure. A circular indentation basically follows the same trend, except that dominant local modes apply to both directions of the plate. For the same given indentation area, a strip indentation seems to outperform its circular counterpart, in terms of both energy focalization and the overall damping enhancement.

As a final remark, Daubechies wavelets, including both highly localized and highly smooth members, are compactly supported and orthogonal. These properties endow them with the ability to capture local structural changes and details, even when the ratio of ABH dimension to the overall structural dimension becomes small. In such cases, one should expect the effective range of the systematic ABH effects to be increased. For a given problem, a possible optimization could be conducted using the present modal to strike a balance between the optimal configuration of the ABH cells (number and size) and the targeted frequency range of interest.

Acknowledgements

Appendix A. formulas for M, K, and F

The plate structure is divided into five parts: uniform parts from 1 to 4 and an ABH part 5.
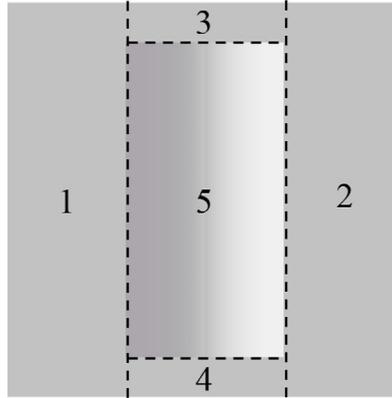
Fig. 16. Division of strip ABH plate.

$$\mathbf{M} = \mathbf{M}^{Uniform} + \mathbf{M}^{ABH} + \mathbf{M}^{Damping}$$

$$\mathbf{K} = \mathbf{K}^{Uniform} + \mathbf{K}^{ABH} + \mathbf{K}^{Spring}$$

$$\mathbf{M}^{Uniform} = \rho hab \left(\sum_{i=1}^{4} \int_{\eta_{i1}}^{\eta_{i2}} \int_{\xi_{i1}}^{\xi_{i2}} \varphi_r(\xi)\varphi_i(\xi)\varphi_s(\eta)\varphi_j(\eta)d\xi d\eta \right)$$
$$= \rho hab \sum_{i=1}^{4} \left(\mathbf{I}_{x_i}^{00} \otimes \mathbf{I}_{y_i}^{00} \right)$$

$$\mathbf{M}^{ABH} = \rho ab \left(\int_{\eta_{51}}^{\eta_{52}} \int_{\xi_{51}}^{\xi_{52}} h(\xi)\varphi_r(\xi)\varphi_i(\xi)\varphi_s(\eta)\varphi_j(\eta)d\xi d\eta \right)$$
$$= \rho ab \left(\mathbf{I}_{x_5}^{00} \otimes \mathbf{I}_{y_5}^{00} \right)$$

$$\mathbf{M}^{Damping} = \rho ab \left(\int_{\eta_{d1}}^{\eta_{d2}} \int_{\xi_{d1}}^{\xi_{d2}} h_d\varphi_r(\xi)\varphi_i(\xi)\varphi_s(\eta)\varphi_j(\eta)d\xi d\eta \right)$$
$$= \rho ab \left(\mathbf{I}_{x_d}^{00} \otimes \mathbf{I}_{y_d}^{00} \right)$$

$$\mathbf{K}^{Uniform} = D\cdot\frac{b}{a^3}\left(\sum_{i=1}^{4}\int_{\eta_{i1}}^{\eta_{i2}}\int_{\xi_{i1}}^{\xi_{i2}}\varphi_r''(\xi)\varphi_i''(\xi)\varphi_s(\eta)\varphi_j(\eta)d\xi d\eta\right) + D\cdot\frac{a}{b^3}\left(\sum_{i=1}^{4}\int_{\eta_{i1}}^{\eta_{i2}}\int_{\xi_{i1}}^{\xi_{i2}}\varphi_r(\xi)\varphi_i(\xi)\varphi_s''(\eta)\varphi_j''(\eta)d\xi d\eta\right)$$

$$+\frac{\mu_0 D}{ab}\left(\sum_{i=1}^{4}\int_{\eta_{i1}}^{\eta_{i2}}\int_{\xi_{i1}}^{\xi_{i2}}\varphi_r''(\xi)\varphi_i(\xi)\varphi_s(\eta)\varphi_j''(\eta)d\xi d\eta\right) + \frac{2(1-\mu_0)D}{ab}\left(\sum_{i=1}^{4}\int_{\eta_{i1}}^{\eta_{i2}}\int_{\xi_{i1}}^{\xi_{i2}}\varphi_r'(\xi)\varphi_i'(\xi)\varphi_s'(\eta)\varphi_j'(\eta)d\xi d\eta\right)$$

$$= D\cdot\frac{b}{a^3}\left(\sum_{i=1}^{4}\mathbf{I}_{x_i}^{22}\otimes\mathbf{I}_{y_i}^{00}\right) + D\cdot\frac{a}{b^3}\left(\mathbf{I}_{x_i}^{00}\otimes\mathbf{I}_{y_i}^{22}\right) + \mu_0 D\cdot\frac{1}{ab}\left(\sum_{i=1}^{4}\mathbf{I}_{x_i}^{20}\otimes\mathbf{I}_{y_i}^{02}\right) + 2(1-\mu_0)D\cdot\frac{1}{ab}\left(\mathbf{I}_{x_i}^{11}\otimes\mathbf{I}_{y_i}^{11}\right)$$

$$\mathbf{K}^{ABH} = \frac{E_0}{12(1-\mu_0^2)}\left\{\int_{\eta_{51}}^{\eta_{52}}\int_{\xi_{51}}^{\xi_{52}}[h(\xi)]^3\left(\begin{array}{l}\frac{b}{a^3}\varphi_r''(\xi)\varphi_i''(\xi)\varphi_s(\eta)\varphi_j(\eta)+\frac{a}{b^3}\varphi_r(\xi)\varphi_i(\xi)\varphi_s''(\eta)\varphi_j''(\eta)\\+\frac{\mu_0}{ab}\varphi_r''(\xi)\varphi_i(\xi)\varphi_s(\eta)\varphi_j''(\eta)+\frac{2(1-\mu_0)}{ab}\varphi_r'(\xi)\varphi_i'(\xi)\varphi_s'(\eta)\varphi_j'(\eta)\end{array}\right)d\xi d\eta\right\}$$

$$= \frac{E_0}{12(1-\mu_0^2)}\left\{\frac{b}{a^3}\left(\mathbf{I}_{x_5}^{22}\otimes\mathbf{I}_{y_5}^{00}\right)+\frac{a}{b^3}\left(\mathbf{I}_{x_5}^{00}\otimes\mathbf{I}_{y_5}^{22}\right)+\frac{\mu_0}{ab}\left(\mathbf{I}_{x_5}^{20}\otimes\mathbf{I}_{y_5}^{02}\right)+\frac{2(1-\mu_0)}{ab}\left(\mathbf{I}_{x_5}^{11}\otimes\mathbf{I}_{y_5}^{11}\right)\right\}$$

$$\mathbf{K}^{Damping} = \frac{E_d}{12(1-\mu_d^2)}\left\{\int_{\eta_{d1}}^{\eta_{d2}}\int_{\xi_{d1}}^{\xi_{d2}}\left\{[2h_d+h(\xi)]^3-[h(\xi)]^3\right\}\left(\begin{array}{l}\frac{b}{a^3}\varphi_r''(\xi)\varphi_i''(\xi)\varphi_s(\eta)\varphi_j(\eta)\\[4pt]+\frac{a}{b^3}\varphi_r(\xi)\varphi_i(\xi)\varphi_s''(\eta)\varphi_j''(\eta)\\[4pt]+\frac{\mu_d}{ab}\varphi_r''(\xi)\varphi_i(\xi)\varphi_s(\eta)\varphi_j''(\eta)\\[4pt]+\frac{2(1-\mu_d)}{ab}\varphi_r'(\xi)\varphi_i'(\xi)\varphi_s'(\eta)\varphi_j'(\eta)\end{array}\right)d\xi d\eta\right\}$$

$$= \frac{E_d}{6(1-\mu_d^2)}\left\{\frac{b}{a^3}\left(\mathbf{I}_{x_d}^{22}\otimes\mathbf{I}_{y_d}^{00}\right)+\frac{a}{b^3}\left(\mathbf{I}_{x_d}^{00}\otimes\mathbf{I}_{y_d}^{22}\right)+\frac{\mu_d}{ab}\left(\mathbf{I}_{x_d}^{20}\otimes\mathbf{I}_{y_d}^{02}\right)+\frac{2(1-\mu_d)}{ab}\left(\mathbf{I}_{x_d}^{11}\otimes\mathbf{I}_{y_d}^{11}\right)\right\}$$

$$\mathbf{K}^{Spring} = k_1 b\varphi_-\otimes\mathbf{I}^{00} + k_2 b\varphi_+\otimes\mathbf{I}^{00} + c_1\frac{b}{a^2}\varphi_-'\otimes\mathbf{I}^{00} + c_2\frac{b}{a^2}\varphi_+'\otimes\mathbf{I}^{00}$$

$$+k_3 a\mathbf{I}^{00}\otimes\varphi_- + k_4 a\mathbf{I}^{00}\otimes\varphi_+ + c_3\frac{a}{b^2}\mathbf{I}^{00}\otimes\varphi_-' + c_4\frac{a}{b^2}\mathbf{I}^{00}\otimes\varphi_+'$$

where $\mathbf{I}^{00} = \int_0^1\varphi_r(\xi)\varphi_i(\xi)d\xi$

$$\varphi_- = [\varphi_r(0)\varphi_i(0)]$$

$$\varphi_+ = [\varphi_r(1)\varphi_i(1)]$$

$$\varphi_-' = [\varphi_r'(0)\varphi_i'(0)]$$

$$\varphi_+' = [\varphi_r'(1)\varphi_i'(1)]$$

$$\mathbf{f}(\mathbf{t}) = \mathbf{F}e^{i\omega t}$$

$$\mathbf{F}_{r,s} = \mathbf{F}\varphi_r(\xi)\varphi_s(\eta)$$

where

$$r = -L+2, -L+1\cdots, 2^m-2, 2^m-1$$

$$i = -L+2, -L+1\cdots, 2^m-2, 2^m-1$$

$$j = -L+2, -L+1\cdots, 2^m-2, 2^m-1$$

$D = \frac{E_0 h^3}{12(1-\mu_0^2)}$ is the bending rigidity of uniform portion of the plate.

Appendix B. Nomenclature

a	Length of the plate
b	Width of the plate
h	Thickness of the uniform portion of the plate
$h(x)$	Variable thickness of the ABH portion
ε	A constant defining the thickness profile
γ	Power law index
h_0	Smallest thickness of the ABH identation
h_d	Thickness of damping layers on each side of plate
k_i	Translational stiffness of the boundary artificial springs
c_i	Rotational stiffness of the boundary artificial springs
E_0	Young's modulus of the plate
E_d	Young's modulus of the damping layers
ρ_0	Mass density of the plate
ρ_d	Mass density of the damping layers
η_0	Loss factor of the plate
η_d	Loss factor of the damping layers
$\{u, v, w\}$	Vector of displacement
ξ, η	Dimensionless coordinates in x and y directions
$a_{ij}(t)$	Generalized coordinates
$\overline{p}, \overline{q}$	Truncation order
$\mathscr{L}$	Lagrangian operator
E_k	Kinetic energy
E_p	Potential energy
W	Work done by external forces
$f(t)$	Excitation force
$\mathbf{M}$	Mass matrix
$\mathbf{K}$	Stiffness matrix
ω	Complex natural angular frequency
ω_n	Natural angular frequency
η_n	Modal loss factor
φ	Daubechies wavelet scaling function
ψ	Mother wavelet function
p_l	Wavelet filter coefficient
L	Even integer
m	Resolution
$\mathbf{I}$	Connection coefficient
$<v_{ABH}^2>$	Mean square velocity of the ABH portion
$<v_{uniform}^2>$	Mean square velocity of the uniform portion
Γ	Mean square velocity ratio
$h(r)$	Thickness of the circular indentation
R_{ABH}	Radius of the circular indentation

References

[1] M.A. Mironov, Propagation of a flexural wave in a plate whose thickness decreases smoothly to zero in a finite interval, Sov. Phys. Acoust. 34 (1988) 318–319.

[2] E.P. Bowyer, D.J. O'Boy, V.V. Krylov, F. Gautier, Experimental investigation of damping flexural vibrations in plates containing tapered indentations of power-law profile, Appl. Acoust. 74 (2013) 553–560.

[3] E.P. Bowyer, V.V. Krylov, Experimental study of sound radiation by plates containing circular indentations of power-law profile, Appl. Acoust. 88 (2015) 30–37.

[4] S.C. Conlon, J.B. Fahnline, F. Semperlotti, Numerical analysis of the vibroacoustic properties of plates with embedded grids of acoustic black holes, J. Acoust. Soc. Am. 137 (2015) 447–457.

[5] D.J. O'Boy, V.V. Krylov, Vibration of a rectangular plate with a central power-law profiled groove by the Rayleigh–Ritz method, Appl. Acoust. 104 (2016) 24–32.

[6] V. Denis, F. Gautier, A. Pelat, J. Poittevin, Measurement and modelling of the reflection coefficient of an acoustic black hole termination, J. Sound Vib. 349 (2015) 67–79.

[7] V. Denis, A. Pelat, F. Gautier, B. Elie, Modal overlap factor of a beam with an acoustic black hole termination, J. Sound Vib. 333 (2014) 2475–2488.

[8] V.V. Krylov, F.J.B.S. Tilman, Acoustic "black holes" for flexural waves as effective vibration dampers, J. Sound Vib. 274 (2004) 605–619.

[9] T. Zhou, L. Tang, H. Ji, J. Qiu, L. Cheng, Dynamic and static properties of double-layered compound acoustic black hole structures, Int. J. Appl. Mech. 9 (2017) 1750074.

[10] L. Zhao, S.C. Conlon, F. Semperlotti, Broadband energy harvesting using acoustic black hole structural tailoring, Smart Mater. Struct. 23 (2014) 65021.

[11] L. Tang, L. Cheng, Enhanced Acoustic Black Hole effect in beams with a modified thickness profile and extended platform, J. Sound Vib. 391 (2017) 116–126.

[12] V.V. Krylov, R.E.T.B. Winward, Experimental investigation of the acoustic black hole effect for flexural waves in tapered plates, J. Sound Vib. 300 (2007) 43–49.

[13] V.V. Krylov, Geometrical-acoustics approach to the description of localized vibrational modes of an elastic solid wedge, Sov. Phys. Tech. Phys. 35 (1990) 137–140.

[14] C. Vemula, A.N. Norris, G.D. Cody, Attenuation of waves in plates and bars using a graded impedance interface at edges, J. Sound Vib. 196 (1996) 107–127.

[15] Y.K. Lin, B.K. Donaldson, A brief survey of transfer matrix techniques with special reference to the analysis of aircraft panels, J. Sound Vib. 10 (1969) 103–143.

[16] S. Félix, V. Pagneux, Multimodal analysis of acoustic propagation in three-dimensional bends, Wave Motion 36 (2002) 157—168.
[17] V.V. Krylov, New type of vibration dampers utilising the effect of acoustic'black holes', Acta Acust. United Acust 90 (2004) 830—837.
[18] L. Tang, L. Cheng, H. Ji, J. Qiu, Characterization of acoustic black hole effect using a one-dimensional fully-coupled and wavelet-decomposed semi-analytical model, J. Sound Vib. 374 (2016) 172—184.
[19] L. Tang, L. Cheng, Broadband locally resonant band gaps in periodic beam structures with embedded acoustic black holes, J. Appl. Phys. 121 (2017) 194901.
[20] S. Zhang, L. Cheng, Wavelet decompositions for high frequency vibrational analyses of plates, Int. J. Appl. Mech. 9 (2017) 1750088.
[21] S. Ilanko, L. Monterrubio, Y. Mochida, The Rayleigh-ritz Method for Structural Analysis, first ed., John Wiley & Sons, Hoboken, 2014.
[22] P. Ruta, Application of Chebyshev series to solution of non-prismatic beam vibration problems, J. Sound Vib. 227 (1999) 449—467.
[23] S. Zhang, L. Cheng, On the efficacy of the wavelet decomposition for high frequency vibration analyses, J. Sound Vib. 380 (2016) 213—223.
[24] L. Cheng, R. Lapointe, Vibration attenuation of panel structures by optimally shaped viscoelastic coating with added weight considerations, Thin-Walled Struct. 21 (1995) 307—326.
[25] M.Q. Chen, C. Hwang, Y.P. Shih, The computation of wavelet-Galerkin approximation on a bounded interval, Int. J. Numer. Meth. Eng. 39 (1996) 2921—2944.